Journal of Molecular Catalysis A: Chemical 339 (2011) 99–107

Contents lists available at ScienceDirect

Journal of Molecular Catalysis A: Chemical

journal homepage: www.elsevier.com/locate/molcata

Theoretical mechanistic study of TangPhos-catalyzed asymmetric γ addition of thiols to allenoates

Nan Lu, Lin Meng, Dezhan Chen*, Guiqiu Zhang

College of Chemistry, Chemical Engineering and Materials Science, Department of Chemistry, Wenhua East Road 88, Shandong Normal University, Jinan 250014, PR China

ARTICLE INFO

Article history:
Received 9 December 2010
Received in revised form 31 January 2011
Accepted 3 March 2011

Keywords:
Lewis base
Nucleophilic catalyst
Chiral phosphine
Addition
Density functional calculation

ABSTRACT

TangPhos-catalyzed asymmetric γ addition of thiols to allenoates has been investigated according to density functional theory. The uncatalyzed addition occurs at β-carbon via a process which involves C–S bond formation and proton transfer from S to γ-carbon. The β-thioester is generated. In TangPhos-catalyzed case, the nucleophilic thiol attacks γ-carbon after the addition of TangPhos to β-carbon. The proton transfers firstly from P of TangPhos to carbonyl O and then to β-carbon. The γ-thioester is obtained. Step1 is rate-limiting. As nucleophilic catalyst, P2 forms strong covalent bond with β-carbon which shifts the positive charge of C2, leaving C3 as the electrophilic center for γ addition. The regioselectivity is consequently altered. As Lewis base, P1 deprotonates thiol enhancing the nucleophility of S and facilitates the proton transfer to β-carbon as a medium. Among four competitive pathways, ER path is the most favorable one with smallest rotation of the single bond linking two chiral rings in TangPhos. The primary domination on enantioselectivity of chiral rings is assisted by *t*-butyl group, which also prefers ER path with the least steric hindrance. Our conclusion is supported by NBO analysis and the predicted ee values according to the experiment.

1. Introduction

During the past several decades, the functionalization of C–H bond by carbon [1,2], nitrogen [3–5], and oxygen [6,7] nucleophiles has been the focus of intense interest. In contrast, relatively little progress has been described in the employment of sulfide as a nucleophile [8,9]. It is particularly valuable since the enantioselective addition to C=S double bond, unlike that to carbonyl or imine [10], is synthetically unavailable. The optically active sulfur-containing compounds, which are difficult to access by other means, have broad applications in chemistry and biology, such as antibiotics [11–13], ligands for metallic catalysts [14,15], organocatalysts [16] and chiral auxiliaries [17].

Deng has achieved the β addition of α,β-unsaturated carbonyl compounds [18,19] via sulfa–Michael reaction [9]. Lu has introduced the addition of electron-deficient alkyne at α position in tandem reactions [4]. In addition, α sulfenylation of aldehyde has already been reported by Jørgensen [8]. As a regiochemical complement, the γ addition of unsaturated carbonyl compounds remains a challenge until Trost discovered the umpolung addition at γ-carbon catalyzed by Ph_3P [20]. As one kind of phosphines, the nucleophilic catalysis of Ph_3P has been widely utilized in α and γ additions to active alkynes and allenes with various pronucleophiles in the earlier researches [21,22]. The major achievements include Zhang's asymmetric synthesis of quaternary carbon center catalyzed by chiral phosphabicyclo [2.2.1]-heptane [1] and inter- [3], intra- [4] molecular γ addition with nitrogen nucleophiles.

At present, Fu group [2,7] has found an array of efficient phosphines as catalysts for various γ addition, which have been employed previously just as chiral ligands for transition metals. For example, binaphthyl-derivated (*S*)-phosphepine has been applied for asymmetric C–C bond formation [2]. An enantioselective synthesis of oxygen heterocycle has been promoted by spiro monophosphine [7]. Another breakthrough was the asymmetric synthesis of γ-thioester [23] catalyzed by chiral bisphosphine TangPhos [24]. Currently, there is no report about detailed mechanistic study. Why is the regioselectivity altered with and without TangPhos?. What is the unique activation mode of TangPhos?. How is the enantioselectivity for asymmetric γ addition of thiols to allenoates dominated in TangPhos-catalyzed case?. We have investigated these issues by means of density functional theory (DFT), which provides an excellent compromise between computational cost and accuracy of outcome [25–29]. Generally, the hybrid functions are accurate enough to describe complexes with H bonds. DFT method is also well-documented for the rationalization and quantitative prediction of stereoselectivity in organocatalysis.

* Corresponding author. Tel.: +86 531 86180304; fax: +86 531 86180304.
E-mail address: dchen@sdnu.edu.cn (D. Chen).

1381-1169/$ – see front matter © 2011 Published by Elsevier B.V.
doi:10.1016/j.molcata.2011.03.003

2. Computational details

Calculations were carried out using the B3LYP [30–32] density functional method as implemented in the Gaussian03 [33] program package. Geometries of all intermediates (IMs) and transition states (TSs) were fully optimized with the 6-31G(d,p) basis set. Frequencies were analyzed at the same level to characterize the nature of stationary points (energy minima or first-order saddle-points) and to provide thermodynamic quantities such as zero-point energy (ZPE) and thermal corrections. Energies were then calculated as single points at B3LYP/6-311++G(d,p), BB1K/6-311++G(d,p) and MP2/6-311++G(d,p) levels [34,35]. The intrinsic reaction coordinate (IRC) paths [36] were also traced to verify the energy profiles which connect each transition state to correct associated local minima.

Meanwhile the basis set superposition error (BSSE) corrections for species were estimated using the counterpoise method [37]. To illustrate the electronic properties and bonding characters for stationary points, natural bond orbital (NBO) analysis was performed at B3LYP/6-311++G(d,p) level [38,39]. To consider the solvent effect on reaction, single-point PCM//B3LYP/6-311++G(d,p) calculations with self-consistent reaction field [40–42] based on polarizable continuum model (PCM) [43,44] were applied for all gas-phase optimized structures. Toluene was chosen as a solvent. For all cited energies, ZPE corrections were taken into account. Since this treatment is somewhat different from the real solution phase condition, our conclusion derived from the present calculation is expected to explain qualitatively the experimental findings.

3. Results and discussion

The mechanism we suggest for the addition process of alkyl thiol **2** to allenoate **1** is outlined in Scheme 1. In the absence of TangPhos (**TP**), the uncatalyzed addition occurs at β position of **1** leading to the β-thioester **3** [23]. In TangPhos-catalyzed process, the nucleophilic addition of TangPhos to β-carbon relatively enhances

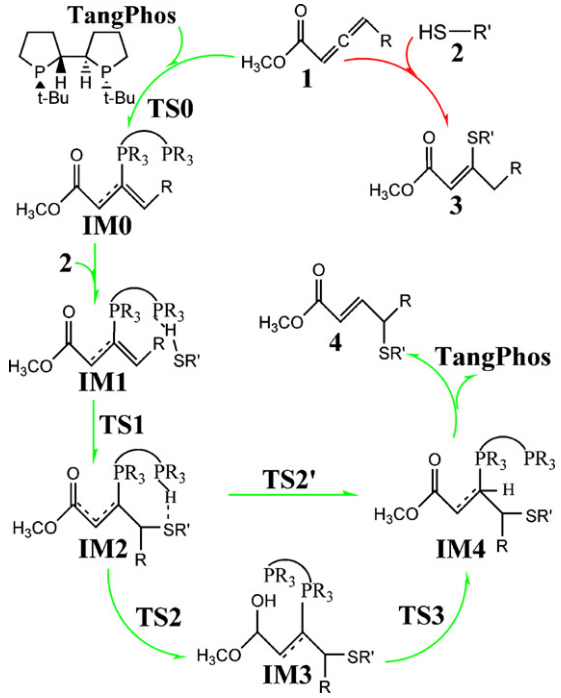

Scheme 1. Proposed mechanistic rationale for the uncatalyzed β addition (red) and TangPhos-catalyzed asymmetric γ addition (green) of thiol to allenoate. (For interpretation of the references to color in this figure legend, the reader is referred to the web version of this article.)

the electrophilicity of γ-carbon in binary complex **IM0**. Then it is readily accessible that the deprotonated **2** attacks γ-carbon by nucleophilic way. From **IM2**, there are two different routes in subsequent catalytic cycle. One is proton transfer firstly from P of TangPhos to the carbonyl O of **1** and then to the β-carbon. The other is a direct hydrogen migration from P of TangPhos to the β-carbon of **1**. Finally, TangPhos and the product γ-thioester **4** [23] are liberated.

3.1. Uncatalyzed addition process

According to our calculation, the uncatalyzed β addition is a stepwise process involving C–S bond formation and proton transfer from S to γ-carbon. In view of E and Z configurations of β-thioester **3**, we located two competitive pathways (denoted as ***β*E**, ***β*Z**), yielding **E-3** and **Z-3**, respectively. The structures of four TSs are shown in Fig. 1 with key atoms numbered. In ***β*E** path, C–S bond is formed as the nucleophilic addition of **2** to **1** takes place via ***β*E-TS1** with a barrier of 24.72 kcal mol^{-1} (Table 1). This step is endothermic by 23.59 kcal mol^{-1} and produces an active intermediate ***β*E-IM2**. Then the proton transfer from S to C3 passes through ***β*E-TS2**, which is higher in energy by 20.89 kcal mol^{-1} than ***β*E-IM2**. The released substantial energy (52.29 kcal mol^{-1}) of step2 facilitates the whole process thermodynamically. In ***β*Z-TS1**, attributed to the steric repulsion resulting from the methyl on C3 directed towards **2**, the barrier of step1 in ***β*Z** path is higher by 7.07 kcal mol^{-1} than that of ***β*E** path (Fig. 2a). Inversely, step2 of ***β*Z** path involves a barrier 3.02 kcal mol^{-1} lower than that of ***β*E** path. From the perspective of rate-limiting step1, the product **E-3** of ***β*E** path is favorable kinetically. Moreover, **E-3** is more stable by 3.11 kcal mol^{-1} than **Z-3**, which also determines that **E-3** is the major thermodynamic product of uncatalyzed β addition.

To verify the reliability of B3LYP method, we carried out single-point calculations for species in ***β*E** path at three different levels (Table 1). Compared with the case of B3LYP, the relative electronic energies of species with BB1K and MP2 methods are lowered at different degrees. The values of two barriers decrease by 0.89 and 1.14 (BB1K); 0.66 and 0.78 kcal mol^{-1} (MP2), respectively. This discrepancy is small so that its influence could almost be omitted. In the following analysis, B3LYP method will be applied to replace the time-consuming MP2 method.

The charge transfer between reactants is known to be a driving force for reaction. We list the partial charge for species of ***β*E** path in Table 2. In ***β*E-IM1**, the charge density centered on C3 (−0.271) is higher than that on C2 (0.125), which is attributed to the electron-withdrawing effect of carbonyl group in **1**. The nucleophilic S (−0.059) always attacks C2 with more positive charge than C3, which interprets the observed regioselectivity of uncatalyzed β addition [23]. In ***β*E-TS1**, the negative charge on C2 as well as C1, C3 and O1 atoms is increased relative to ***β*E-IM1**. The electronegative S atom (−0.059) in ***β*E-IM1** becomes greatly electropositive (0.619) in ***β*E-IM2**, where C2 is thoroughly electronegative (−0.198), which is the result of charge transfer from **2** to **1**. In ***β*E-TS2**, as the proton transfers from S to C3, the charge density on C3 should be decreased. While in step2, as the sp2 hybridization of C3 turns to sp3, the conjugated effect between O1 and C3 is disappearing. This diminishes remarkably the influence of electron-withdrawing effect of carbonyl group on C3. Therefore the charge density on C3 is increased (−0.216 → −0.424) instead.

To make a comprehensive analysis of the regioselectivity in uncatalyzed case, we locate TSs (Fig. 1) leading to four configurations of γ-thioester **4** in terms of double bond and chiral carbon. In four corresponding pathways (denoted as ***γ*ER**, ***γ*ES**, ***γ*ZR** and ***γ*ZS**), the C3–S bond formation occurs concertedly with proton transfer from S to the β-carbon. Although the attack orientation of **2** to **1** is different from each other, four paths are of close energy barriers

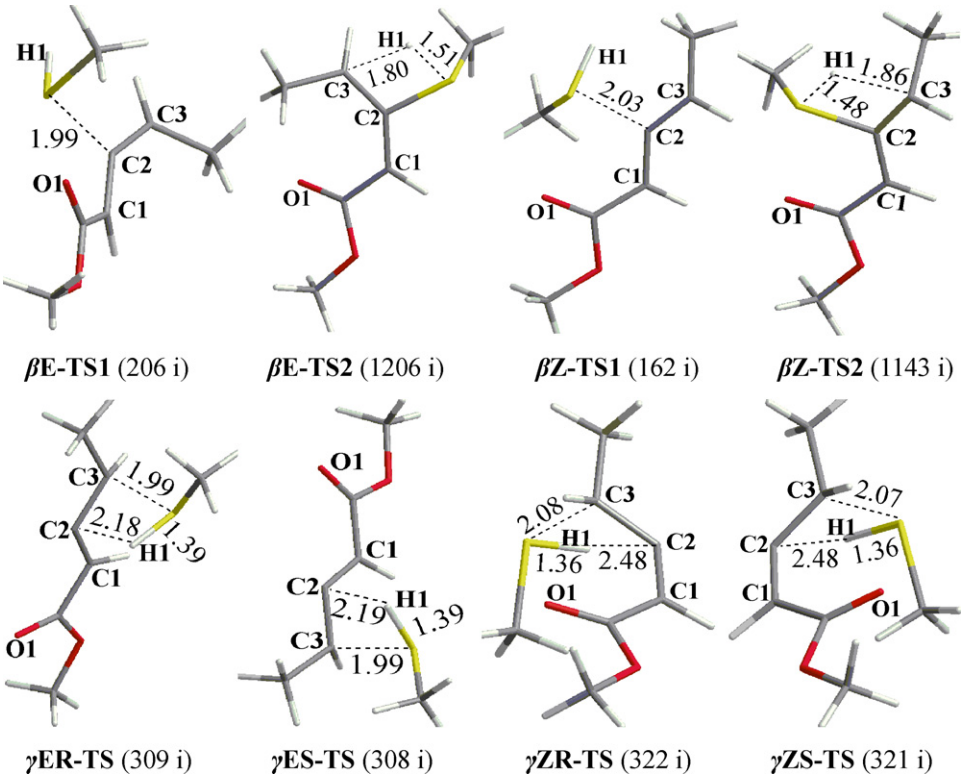

Fig. 1. Optimized structures of TSs in uncatalyzed β and γ addition of alkyl thiol to allenoate (bond length in Å; the imaginary frequency (cm^{-1}) in parentheses).

Table 1
Relative electronic energy considering ZPE corrections (kcal mol^{-1}) of species in ***β*E** pathway at three different levels (italic values are real energies (a.u.)).

Species	ZPE	B3LYP/6-311++G(d,p)	BB1K/6-311++G(d,p)	MP2/6-311++G(d,p)
1 + 2	0.17492	*−822.362776*	*−822.259158*	*−820.483506*
		0	0	0
***β*E-IM1**	0.17546	0.54	0.35	−1.75
***β*E-TS1**	0.17725	25.26	24.18	22.31
***β*E-IM2**	0.17832	24.13	23.76	22.12
***β*E-TS2**	0.17407	45.02	43.51	42.23
***β*E-IM3**	0.18279	−28.16	−28.63	−29.55

with not more than 1 kcal mol^{-1} (Fig. 2a) differences. The barriers of γ addition are approximately 30 kcal mol^{-1} higher than those of β addition. This fact suggests that the uncatalyzed γ addition is impossible. Our calculation further supports the experimental results.

3.2. TangPhos-catalyzed asymmetric γ addition

TangPhos is a chiral bisphosphine originally developed as a ligand for Rh-catalyzed reaction. The backbone of this new organocatalyst is characterized by two chiral carbons which link two five-membered phospholane rings and two *t*-butyl groups. This structure restricts its conformational flexibility and accordingly exhibits a chiral environment, which is desired in enantioselective reaction. Besides, the two phosphorus centers enable it to be nucleophilic catalyst and Lewis base.

3.2.1. Frontier molecular orbital analysis

To understand the initial role of TangPhos in γ addition, a frontier molecular orbital (FMO) analysis [45] is made for **1**, **2**, **TP** and

Table 2
Calculated partial charge from NBO analysis.

	C1	C2	C3	O1	S	H1	P1 (0.4206)	P2
***β*E-IM1**	−0.406	0.125	−0.271	−0.600	−0.059	0.252		
***β*E-TS1**	−0.526	−0.058	−0.326	−0.717	0.505	0.118		
***β*E-IM2**	−0.573	−0.198	−0.261	−0.677	0.619	0.126		
***β*E-TS2**	−0.470	−0.144	−0.424	−0.639	0.508	0.169		
ER-IM1	−0.535	−0.371	−0.252	−0.768	−0.078	0.145	0.808	1.634
ER-TS1	−0.453	−0.613	−0.171	−0.818	−0.287	0.062	1.350	1.640
ER-IM2	−0.377	−0.720	−0.328	−0.825	0.138	0.021	1.359	1.622
ER-TS2	−0.524	−0.729	−0.277	−0.848	−0.004	0.117	1.352	1.615
ER-IM3	−0.431	−0.771	−0.328	−0.746	0.140	0.515	0.835	1.604
R-TS3	−0.515	−0.763	−0.344	−0.757	0.208	0.456	0.863	1.620
ER-TS2′	−0.542	−0.760	−0.318	−0.819	0.123	0.102	1.293	1.652

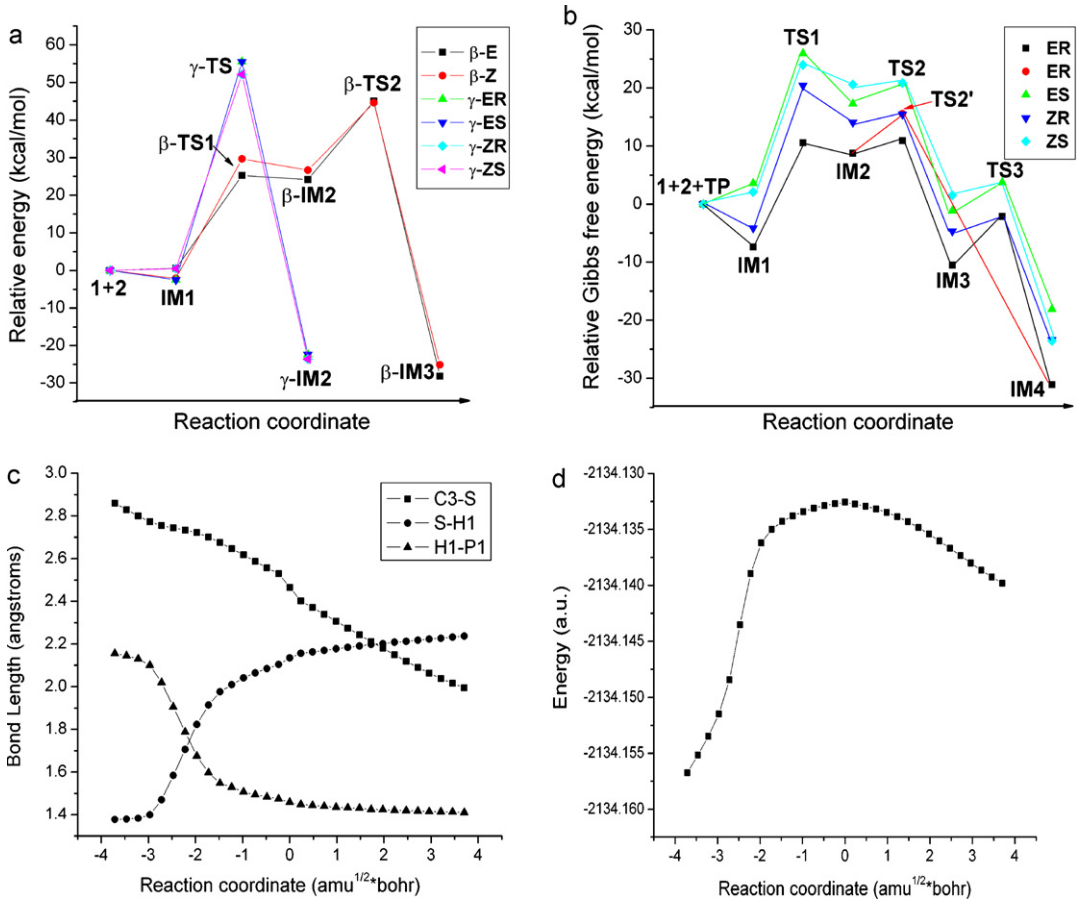

Fig. 2. (a) Relative energy profiles of the uncatalyzed β and γ addition in different pathways. (b) Relative Gibbs free energy profiles of four pathways in TangPhos-catalyzed asymmetric γ addition in solution phase. Evolution of the (c) bond lengths and (d) energy changes along the IRC for **ES-TS1** at B3LYP/6-31G(d,p) level.

the original **IM0** in four paths (Fig. 3a). In FMO theory, the reactivity between two molecules is inversely proportional to the energy difference between the highest occupied molecular orbital (HOMO) of one molecule and the lowest unoccupied molecular orbital (LUMO) of the other. The smaller the HOMO–LUMO difference is, the more reactive the reaction will be. As the HOMO**2**–LUMO**1** difference is smaller than that of HOMO**1**–LUMO**2**, the addition of **2** to **1** will proceed via HOMO**2**–LUMO**1** interaction. The large value (9.78 eV) may account for the observed difficulty of uncatalyzed γ addition. In the presence of TangPhos, the small HOMO**TP**–LUMO**1** difference (6.57 eV) makes the addition of TangPhos to **1** via **TS0** (Fig. 3b) much more accessible. The barrier calculated (13.92 kcal mol^{-1}) is much lower than that of uncatalyzed addition process (25–55 kcal mol^{-1}).

In the resultant **IM0**, HOMO and LUMO energies rise significantly compared with those of **1**. The main interaction turns to HOMO**1**–LUMO**2** with the value reduced to 3.2 eV, implying that the TangPhos-catalyzed asymmetric γ addition will take place easily just as the experiment [23]. The small discrepancy of HOMO–LUMO difference among four **IM0** indicates that four paths are all possible for the catalytic γ addition. Promoted by TangPhos, the barrier of nucleophilic addition of **2** to **1** will be greatly reduced.

3.2.2. Reaction mechanism

From **IM0**, we characterized four paths, of which the relative Gibbs free energy profiles in solution phase are depicted in Fig. 2b. Considering the analogous reaction process of four paths,

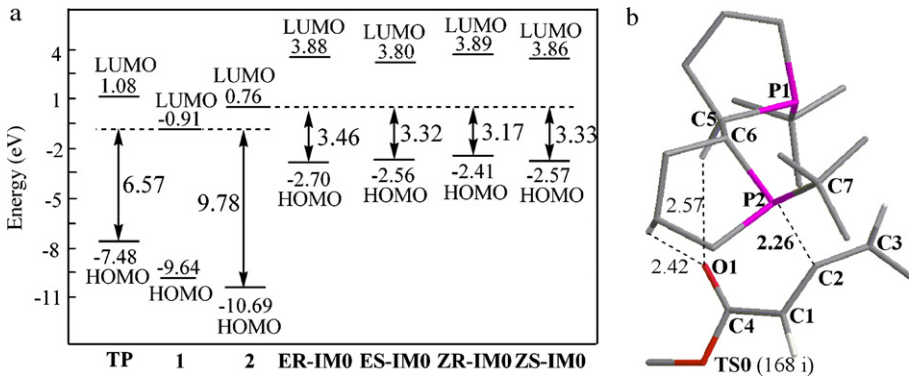

Fig. 3. (a) Energies of the HOMOs and LUMOs for **TP**, **1**, **2** and the original binary complexes **IM0** in four paths. (b) Optimized structure (bond length in Å) of **TS0** in TangPhos-catalyzed asymmetric γ addition of alkyl thiol to allenoate.

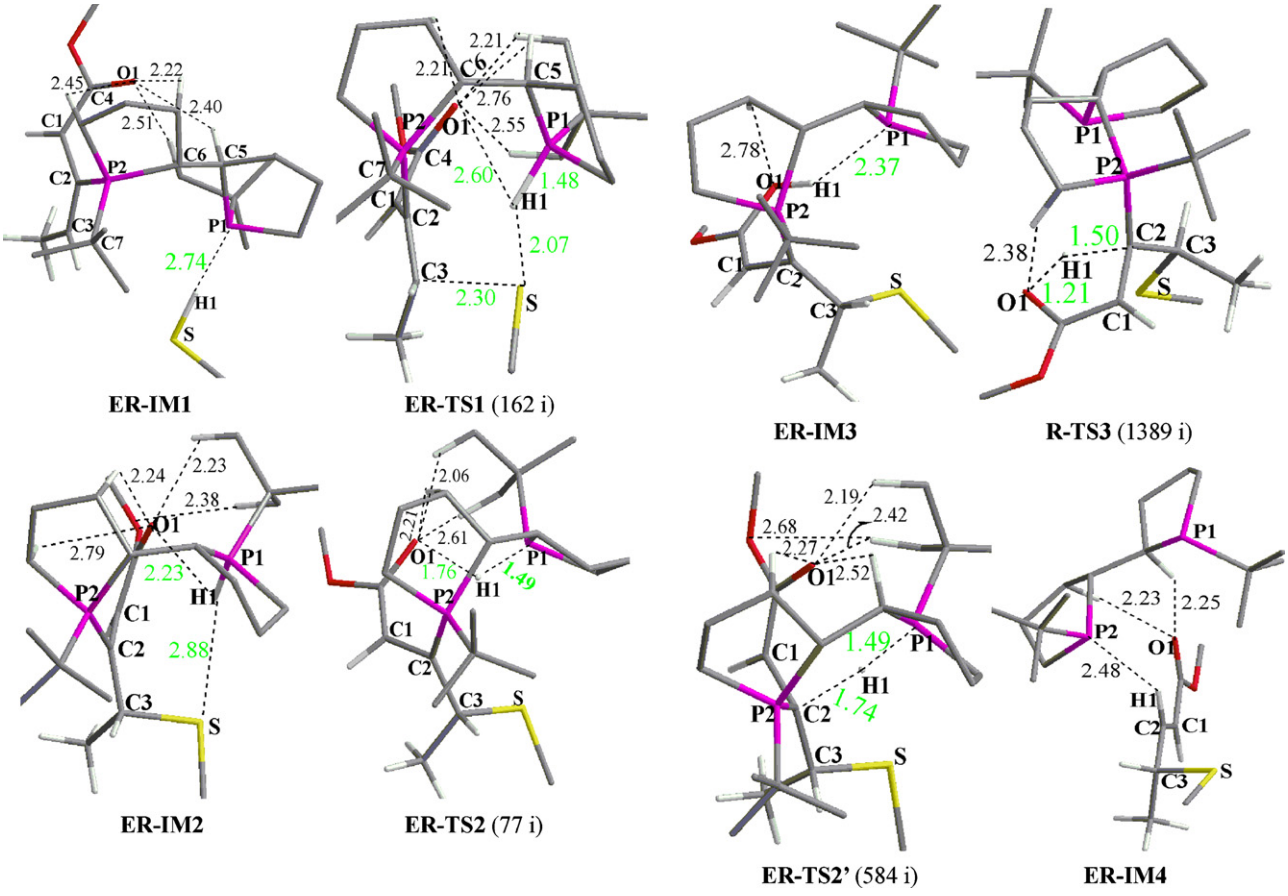

Fig. 4. Optimized structures (bond length in Å) of species in **ER** path in TangPhos-catalyzed asymmetric γ addition of alkyl thiol to allenoate (only key hydrogen atoms are left for clarity. The imaginary frequency (cm^{-1}) of TS is in parentheses). (For interpretation of the references to color in text, the reader is referred to the web version of this article.)

we choose **ER** path to analyze the detailed mechanism. Optimized structures of species in this path are displayed in Fig. 4. In each structure, besides general H bonds (in green), there is a H-bonded network (in black) formed by C–H on the five-membered ring or *t*-butyl group and two ester O atoms of **1**. Table 3 illustrates five types of energy properties for comparison. We use relative Gibbs free energy obtained from PCM//B3LYP/6-311++G(d,p) calculations as following. Toluene ($\varepsilon = 2.38$) was chosen as a solvent according to experiment.

In step1, as **2** approaches **ER-IM0**, a pre-reactive complex **ER-IM1** is formed with a S–H1···P1 H bond distance of 2.74 Å. The formation of C3–S bond proceeds with the deprotonation of **2** by Lewis base P1 occurring concertedly in **ER-TS1**, where the higher charge density on C2 (−0.613) than C3 (−0.171) verifies the nucleophilic addition at C3 (Table 2). From **ER-IM1** to **ER-TS1**, the increased positive charge on P1 (0.808 → 1.350) makes S a more electronegative (−0.078 → −0.287) nucleophilic center. Lengths of the forming C3–S, H–P1 and the breaking S–H1 bonds

Table 3
Relative energy properties (kcal mol^{-1}) of species in four pathways of TangPhos-catalyzed asymmetric γ addition (italic values are real energies (a.u.); corresponding values of **ZR** and **ZS** pathways are in parentheses).

	[a] ΔE_{gas}	[b] ΔE_{gas}^{CP+ZPE}	[c] ΔG_{gas}^{298}	[d] ΔE_{PCM}^{298}	[e] ΔG_{PCM}^{298}
1 + 2 + TP	*−2133.678348*	*−2133.663567*	*−2133.733388*	*−2133.928130*	*−2133.991960*
	0	0	0	0	0
ER(ZR)-IM1	−3.95(1.65)	−3.23(1.96)	−6.49(−2.38)	−3.62(1.22)	−7.38(−4.12)
ER(ZR)-TS1	17.37(19.30)	20.31(22.16)	20.05(21.73)	10.40(20.47)	10.56(20.42)
ER-IM2	9.66	11.49	10.92	8.73	8.73
ER-TS2	8.83	10.42	10.26	9.64	10.90
ER-IM3	−11.52	−9.67	−11.21	−9.43	−10.51
R-TS3	−7.49	−4.97	−5.95	−1.78	−2.13
ER-IM4	−32.55	−28.19	−34.12	−25.75	−31.10
ER-TS2′	12.13	14.20	16.05	13.80	15.56
ES(ZS)-IM1	3.42(7.03)	3.94(8.19)	1.72(2.59)	8.12(6.57)	3.57(2.08)
ES(ZS)-TS1	27.43(22.94)	31.31(26.38)	30.36(23.40)	26.35(23.39)	25.92(23.96)

[a] Relative absolute electronic energy at B3LYP/6-311++G(d,p) level in gas phase.
[b] "a" considering BSSE and ZPE corrections.
[c] Relative Gibbs free energy in gas phase.
[d] Relative electronic energy at PCM//B3LYP/6-311++G(d,p) level in solution phase.
[e] Relative Gibbs free energy in solution phase.

are 2.30, 1.48 and 2.07 Å, respectively. Step1 is endothermic by 16.11 kcal mol^{-1} with a barrier of 17.94 kcal mol^{-1}. In **ER-IM2**, H1 is completely transferred to P1 and the O1···H1 distance is shortened by 0.37 Å from **ER-TS1**. There is also an evident charge transfer from S (−0.287 → 0.138) to C3 (−0.171 → −0.328) compared with **ER-TS1**. The regioselectivity is consequently altered with the formation of C3–S bond. Fig. 2c provides a detailed description of the atomic motion during the course of step1 in **ES** path. Essentially, the process can be described as two internal modes of transformation. One is the hydrogen migration from S of **2** to P1 of TangPhos, which is characterized by the variation of S–H1 and H1–P1 bond lengths. The other involves the formation of a single bond between S of **2** and C3 of **1**, which can be followed by the changes of C3–S bond length. It is clear from the plots that the geometrical parameters do not change gradually and simultaneously as the reaction proceeds. Instead, the hydrogen migration from S to P1 is followed by the C3–S bond formation, which reveals that step1 is concerted and asynchronous. Fig. 2d presents the energy changes from the IRC analysis of **ES-TS1**.

TangPhos is distorted along with the C5–C6 single bond in **ER-TS2**, where the distances of P1···H1···O1 are 1.49 and 1.67 Å. This facilitates the proton transfer from P1 to O1 in step2. Compared with species of step1, the H-bonded network of step2 is weakened. **ER-IM3** is stable with the O1–H1···P1 H bond distance of 2.37 Å. Step2 is exothermic by 19.24 kcal mol^{-1} with a small barrier of 2.17 kcal mol^{-1}. Accordingly step3 could be readily initiated, that is **ER-IM3** undergoes proton transfer from O1 to C2 via **R-TS3**, in which the distances of O1···H1···C2 are 1.21 and 1.50 Å. The structures of **TS3** we located in **ZR** and **ZS** paths are quite analogous to those of **ER** and **ES** paths. The positive charge C2 obtained from H1 is shifted to P2 in majority, which causes P2 to be more electropositive (1.604 → 1.620) and C2 slightly less electronegative (−0.771 → −0.763). With a barrier of 8.38 kcal mol^{-1} in step3, the rate-limiting step of the whole process is step1 undoubtedly. The stable **ER-IM4** (−31.1 kcal mol^{-1}) not only facilitates step2 but also pulls forward the entire reaction efficiently. In the end, the H-bonded network of **ER-IM4** is dissociated giving ER-**4** and the recovered TangPhos.

The alternate route step2′ is a direct hydrogen migration from P1 to C2 via **ER-TS2′**, which is confirmed as a first-order saddle-point connecting **ER-IM2** and **ER-IM4** in IRC analysis. Compared with **ER-TS2**, there is a more compact H-bonded network in **ER-TS2′**, where the distances of P1···H1···C2 are 1.49 and 1.74 Å. In step2′, the positive charge attracted by P2 (1.622 → 1.652) from H1 is more than that of step3. This even makes C2 more electronegative (−0.720 → −0.760) and it could be ascribed to the direct proton shift model without O1 as a medium. The barrier of step2′ is higher by 4.66 kcal mol^{-1} than that of step2. Together with our failed attempt to optimize TSs like **ER-TS2′** in the other three paths, we ensure that the TangPhos-catalyzed asymmetric γ addition consists of three steps with step1 rate-limiting.

From the variation of charge density on P1 and P2 in the whole process, the unique activation mode of TangPhos is clear. Compared with the value on P of the isolated TangPhos (0.421), the positive charge on P2 is as 1.6 high all the time, which is the result of covalent C2–P2 bond that arises from the nucleophilic addition of TangPhos to **1**. As nucleophilic catalyst, P2 effectively shields C2 so that it induces the exposure of C3 for γ addition. When it comes to P1, the positive charge varies between 0.8 and 1.3 during the proton transfer from **2** to **1** mediated by P1. As Lewis base, P1 enhances the nucleophility of **2** which significantly reduces the barrier of γ addition. Two available P sites of TangPhos are crucial for the activation of two reactants in γ addition.

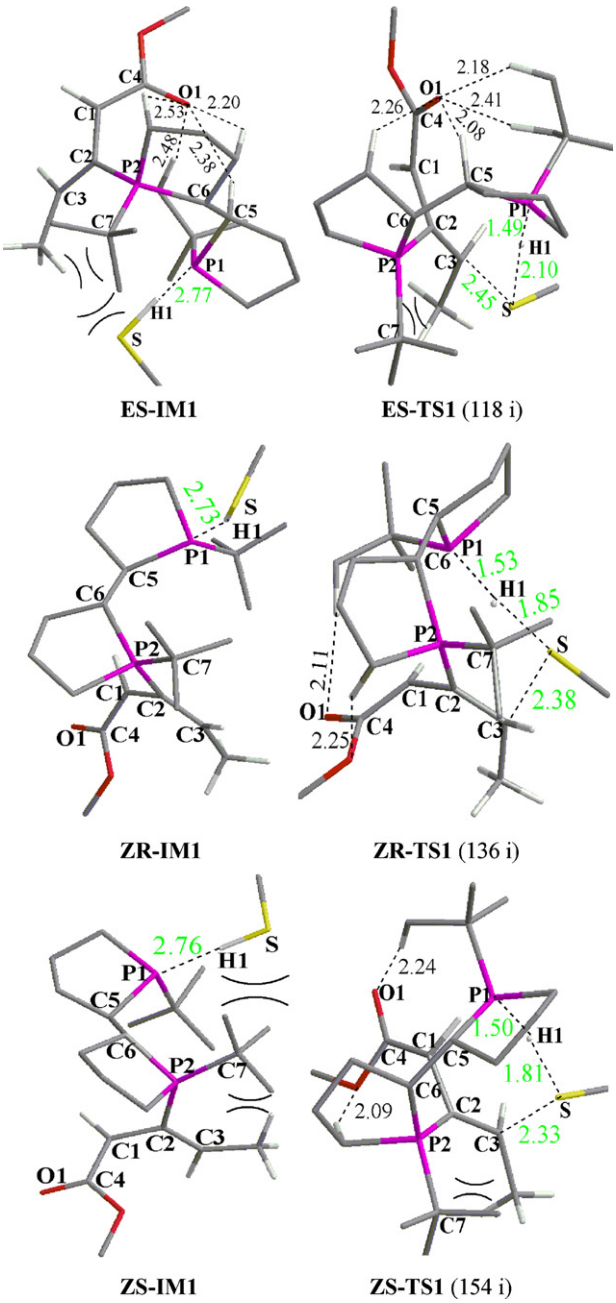

Fig. 5. Optimized structures (bond length in Å) of **IM1** and **TS1** in **ES**, **ZR** and **ZS** pathways in TangPhos-catalyzed asymmetric γ addition of alkyl thiol to allenoate (only key hydrogen atoms are left for clarity. The imaginary frequency (cm^{-1}) of TS is in parentheses.).

3.2.3. Enantioselectivity

3.2.3.1. Characteristic of IM1 and TS1. Since the enantioselectivity is determined in rate-limiting step, a detailed investigation on step1 of four paths is worthwhile. Fig. 5 exhibits the optimized structures of **IM1** and **TS1** in **ES**, **ZR** and **ZS** paths. Despite similar H-bonded network in **ER** and **ES** paths, the steric repulsions between methyl on C3 and *t*-butyl group on P2 as well as thiol **2** make **ES-IM1** 10.95 kcal mol^{-1} higher in energy than **ER-IM1** (Table 3). Although the repulsion intensity in **ES-TS1** is reduced, **ER-TS1** is still more stable owing to a relatively compact structure which involves close distance of O1···H1 (2.6 Å) and shorter length of the forming C3–S bond. Compared with **ES** path (22.35 kcal mol^{-1}), the smaller barrier of **ER** path (17.94 kcal mol^{-1}) ensures kinetically the preference of ER-**4**, which is also more stable than ES-**4** (Fig. 2b). As to **ZR** and

Table 4
The selected dihedral angles (°) of **IM1** and **TS1** in four pathways of TangPhos-catalyzed asymmetric γ addition (changes from **IM1** to **TS1** in parentheses).

	D1 P1–C5–C6–P2	D2 C7–P2–C2–C3	D3 P2–C2–C1–C4
ER-IM1	−49.35	−26.59	41.11
ER-TS1	−19.33	−16.22	42.41
	(30.02)	(10.37)	(1.30)
ES-IM1	−53.11	−33.53	53.04
ES-TS1	17.29	7.12	67.27
	(70.40)	(40.65)	(14.23)
ZR-IM1	−78.94	15.43	−113.80
ZR-TS1	39.77	−8.22	−94.59
	(118.71)	(−23.65)	(19.21)
ZS-IM1	−67.09	7.09	−107.91
ZS-TS1	36.42	−11.03	−96.04
	(103.51)	(−18.12)	(11.87)

ZS paths, O1 is directly opposite to S thereby far from two five-membered rings, which causes the H-bonded network nonexistent in **IM1** and weak in **TS1**. Energy differences of two paths are still related to the steric repulsion of different extent mentioned above. As is severe in **ZS-IM1**, it is less stable by 6.20 kcal mol^{-1} than **ZR-IM1**. As is mild in **ZS-TS1**, it is less stable by 3.48 kcal mol^{-1} than **ZR-TS1**. Therefore, the barrier of **ZR** path (24.54 kcal mol^{-1}) is higher than **ZS** path (21.88 kcal mol^{-1}). Although ZS-**4** almost equals to ER-**4** in energy, ZS-**4** is preferential from the kinetics point of view. On the basis of energy barriers, **ER** and **ZS** paths are selected at first. The most favored **ER** path is eventually determined by the *t*-butyl group via exerting larger steric hindrance in **S** path instead of **R** one.

The enantioselectivity is quantitatively indicated by enantiomeric excess (ee) of an isomer, which is measured by chiral column chromatography and NMR spectroscopy in experiment. Here, based on the transition state theory [46], ee value of R-**4** in solution phase is predicted by employing energy barriers of step1 with the following formula [47]. The calculated ee value 90.1% is in a good agreement with the experimental data ranging from 85% to 95% [23].

$$\frac{[R]}{[S]} = \frac{\exp(-\Delta G_{ER}^{\neq}/RT) + \exp(-\Delta G_{ZR}^{\neq}/RT)}{\exp(-\Delta G_{ES}^{\neq}/RT) + \exp(-\Delta G_{ZS}^{\neq}/RT)} \quad (1)$$

$$\text{ee } (\%) = \frac{[R]-[S]}{[R]+[S]} \times 100 \quad (2)$$

To research the role of chiral environment which derived from TangPhos backbone on enantioselectivity, we summarize the changes of three dihedral angles (ΔD) from **IM1** to **TS1** in step1 (Table 4). The smaller the dihedral angles change, the easier the reaction proceeds [47]. In **ER** path, the values of three ΔD are much smaller than the relevant data of **ES** path. This makes **ER** path far more readily accessible than **ES** path. In contrast, ΔD(**ZR**) is slightly higher than ΔD(**ZS**) which causes **ZS** path a little more favorable than **ZR** path. With a discrepancy of biased extent, the product R-**4** is ultimately favored over its isomer. Then we study separately about the function of five-membered ring (D1), *t*-butyl group (D2) and reactants (D3) on enantioselective control. A larger variation of the dihedral angle denotes a bigger function of the corresponding unit [47]. The magnitude order is $\Delta D1 > \Delta D2 \gg \Delta D3$ in **ER** and **ES** paths; $\Delta D1 \gg \Delta D2 > \Delta D3$ in **ZR** and **ZS** paths. An integral analysis of this fact indicates that enantioselectivity is dominated primarily by two chiral five-membered rings as well as the assistance of *t*-butyl group. Firstly, two chiral rings orient the reaction in **ER** and **ES** paths with smaller rotations of the linked single bond. A second comparison confirms that **ER** path is the most favorable one.

3.2.3.2. Natural bond orbital analysis. NBO analysis, which gives a better description of the electron distribution and bonding characteristics in complex, has been performed to get more qualitative evidence of the structural analysis above. Table 5 exhibits the major bond orders (BOs) and second-order perturbation energies ($E_{i\to j^*}^{(2)}$) of **TS1** in four paths. The relationship between enantioselectivity and four TSs would be validated with the assistance of Wiberg bond index matrix [48] and $E_{i\to j^*}^{(2)}$ [49].

In four paths, BO values of H1–P1 bond are bigger than those of C3–S. It shows that H1–P1 bond is formed earlier than C3–S bond. This reveals that once **2** is deprotonated by Lewis base P1, the nucleophilic addition of S to C3 takes place easily. That is the activation of alkyl thiol by TangPhos. The BO values of C3–S are 0.505, 0.458, 0.462 and 0.486 in **ER-TS1**, **ES-TS1**, **ZR-TS1** and **ZS-TS1**, demonstrating that C3–S bond is formed orderly in **ER**, **ZS**, **ZR**, **ES** paths. $E_{i\to j^*}^{(2)}$, an evaluation of the delocalized energy arising from donor–acceptor interactions is proportional to the overlap integral, which is enlarged with the increase of delocalization of lone pair orbital in an electronegative atom. The superposition between the anti-bonding σ^* orbital of C3–C2 bond and the lone pair orbital of S is closely related with $E_{i\to j^*}^{(2)}$ $\{n(S) \to \sigma^*(C3–C2)\}$, of which the magnitude order is uniform with that of BO value of C3–S bond in four paths. This result illuminates that the interaction energy is the largest in **ER-TS1**, in which the carbon σ^* orbital could accept more electron density than the other three TSs. In **ER-TS1** and **ES-TS1**, BO values of H1–P1 are more by 0.1 than those of **ZR-TS1** and **ZS-TS1**. The case of S–H1 is just opposite. This suggests that compared with **Z** paths, the migration of H1 from S to P1 is more inclined to occur in **E** paths, in which **ER** path is superior to **ES** one. Donor–acceptor charge transfer delocalization also exists between anti-bonding σ^* orbital of H1–P1 and the lone pair orbital of S as well as O1 atom. The H-bond interaction expressed by $E_{i\to j^*}^{(2)}$ $\{n(S) \to \sigma^*(H1–P1)\}$ is the largest in **ER-TS1** which even contains the $E_{i\to j^*}^{(2)}$ $\{n(O1) \to \sigma^*(H1–P1)\}$(0.66 kcal mol^{-1}) that are not existing in the other three TSs. Subsequently, the migrating H1 is stabilized most effectively by charge density on S and O1 in **ER** path.

Table 5
Bond orders (BO) and the second order perturbative energies $E_{i\to j^*}^{(2)}$ (kcal mol^{-1}) of major donor-acceptor interactions in four structures of **TS1** in TangPhos-catalyzed asymmetric γ addition.

	ER-TS1	**ES-TS1**	**ZR-TS1**	**ZS-TS1**
C3–S	0.505	0.458	0.462	0.486
S–H1	0.071	0.160	0.225	0.232
H1–P1	0.852	0.798	0.690	0.741
P2–C2	1.123	1.084	1.095	1.098
C2–C3	1.400	1.309	1.343	1.351
$E_{i\to j^*}^{(2)}$ $\{n(S) \to \sigma^*(C3–C2)\}$	11.11	3.89	4.65	7.83
$E_{i\to j^*}^{(2)}$ $\{n(S) \to \sigma^*(H1–P1)\}$	6.38	2.58	4.43	5.61
$E_{i\to j^*}^{(2)}$ $\{n(O1) \to \sigma^*(H1–P1)\}$	0.66	–	–	–
$E_{i\to j^*}^{(2)}$ $\{\sigma(C2–C3) \to \sigma^*(P2–C2)\}$	2.95	2.68	2.62	2.76
$E_{i\to j^*}^{(2)}$ $\{\sigma(P2–C7) \to \sigma^*(P2–C2)\}$	2.37	2.11	1.93	2.13

In four TSs, BO values of P2–C2 (1.08–1.12) exceed the range of normal single bond (0.9–1.0). The C2–C3 bond is characterized by BO values 1.3–1.4 which are lower than the value of double bond. This clarifies the activation of allenoate by TangPhos that is, as nucleophilic catalyst, P2 forms strong covalent bond with C2 which shifts the positive charge on C2, leaving C3 as the electrophilic center for γ addition. The sum of BO values between P2–C2 and C2–C3 is in order of **ER-TS1** (2.523), **ZS-TS1** (2.449), **ZR-TS1** (2.438), **ES-TS1** (2.393), which explains the stabilization sequence of four paths (**ER** > **ZS** > **ZR** > **ES**) induced by covalent interactions. The donor–acceptor interactions between bonding σ orbital of C2–C3, P2–C7 and anti-bonding σ* orbital of P2–C2 could be denoted by $E^{(2)}_{i\to j^*}$ {σ(C2–C3) → σ*(P2–C2)} and $E^{(2)}_{i\to j^*}$ {σ(P2–C7) → σ*(P2–C2)}, the sum of which is arranged as **ER** > **ZS** > **ES** > **ZR**. Obviously, the stabilization effect of charge transfer delocalization is the largest in **ER** path. The conclusion obtained from BO and $E^{(2)}_{i\to j^*}$ advocates that **ER** path is the most preferential one in TangPhos-catalyzed asymmetric γ addition.

3.2.3.3. Substituent effect. In experiment, much effort has been focused on the scope of allenoates and thiols in catalytic γ addition [23]. The substituent effect of reactants also attracts our attention. In the chiral environment endowed by TangPhos, whether the enantioselectivity could be improved with sterically demanding substrates is still a question. The reaction of *n*-Pr allenoate and phenyl thiol is taken as a model with the optimized structures of **sub-TS1** in four paths depicted in Fig. 6.

Compared with **TS1** in reactions of **1** and **2**, lengths of the forming C3–S bond are all shortened especially the nearly formed H1–P1 bond in **sub-TS1**, the structure of which is more product-like than **TS1**. The phenomenon denotes an easier leaving of H1 from S to P1 accordingly promoting the nucleophilic attack of S–C3. This is presumably resulted from the enhanced steric repulsion between bulky phenyl ring and *n*-Pr group. Moreover, the distances of O1···H1 in **sub-ER-TS1** and **sub-ES-TS1** are much shorter than those of **ER-TS1** and **ES-TS1**. The weak H-bonded network in **ZR-TS1** becomes extremely strong in **sub-ZR-TS1**. Since the O1···H1 distance and H-bonded network are key factors in stabilization, thereby the energy of **sub-TS1** and barriers of four paths are both decreased. We are delighted to find that the preferential order of four paths is retentive and the enantioselectivity of R-**4** is increased to 94.3% ee, which is close to the tiptop of experimental value (95%) [23].

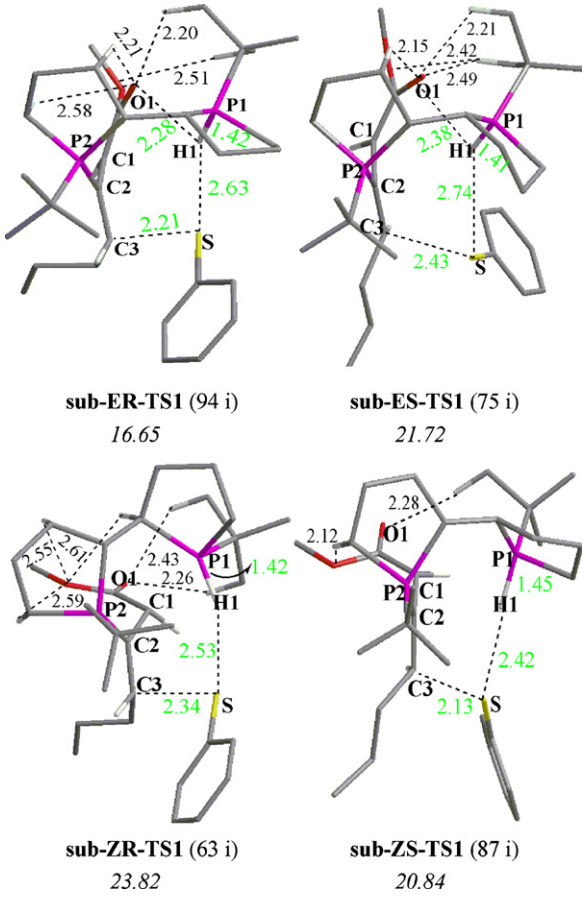

Fig. 6. Optimized structures (bond length in Å) of **sub-TS1** in four pathways of TangPhos-catalyzed asymmetric γ addition of phenyl thiol to *n*-Pr allenoate (only key hydrogen atoms are left for clarity. The imaginary frequency (cm^{-1}) of TS is in parentheses. Energy barriers of the corresponding pathways (kcal mol^{-1}) are shown in italic).

4. Conclusion

Our DFT calculations provide the first theoretical investigation on TangPhos-catalyzed asymmetric γ addition of thiols to allenoates. Without TangPhos, the uncatalyzed addition occurs at β-carbon via a stepwise process involving C–S bond formation and proton transfer from S to γ-carbon which generates β-thioester. TangPhos-catalyzed asymmetric γ addition consists of three steps: the nucleophilic attack of thiol to γ-carbon of allenoate after the addition of TangPhos to β-carbon, the proton transfer firstly from P of TangPhos to the carbonyl O of allenoate, and then to the β-carbon. Step1 is rate-limiting. Finally TangPhos and the product γ-thioester are liberated.

Two P sites of TangPhos are crucial for the activation of reactants in asymmetric γ addition. As nucleophilic catalyst, P2 forms strong covalent bond with β-carbon of allenoate. The P2–C2 bond shifts the positive charge on C2, thus it effectively shields the electrophilic possibility of β-carbon and relatively increases the electrophilicity of C3. With γ-carbon as electrophilic center, the regioselectivity is consequently altered. As Lewis base, P1 deprotonates thiol enhancing the nucleophility of S and facilitates the proton transfer to β-carbon as a medium. Thanks to the two P sites, the barrier of asymmetric γ addition is lowered significantly in TangPhos-catalyzed case.

The research on four competitive paths elucidates that the enantioselectivity is dominated primarily by two chiral five-membered rings as well as the assistance of *t*-butyl groups in TangPhos. Two chiral rings orient the reaction in **ER** and **ES** paths with smaller rotations of the linked single bond. The second comparison confirms that **ER** path is the most favorable one. Via exerting larger steric hindrance in **S** path, *t*-butyl group selects **ER** and **ZS** paths with smaller barriers at first, and the most preferential **ER** path is finally determined. NBO analysis also validates that **ER** path is the most stable one from electron distribution perspective. Two ee values of (R)-γ-thioester (90.1%, 94.3%) are both in the range of experimental data.

Acknowledgements

This work was supported by National Basic Research Program of China (973 Program, 2007CB936000), National Natural Science Foundation of China (No. 20975064) and Natural Science Foundation of Shandong Province (No. ZR2009BZ003).

Appendix A. Supplementary data

Supplementary data associated with this article can be found, in the online version, at doi:10.1016/j.molcata.2011.03.003.

References

[1] Z. Chen, G. Zhu, Q. Jiang, D. Xiao, P. Cao, X. Zhang, J. Org. Chem. 63 (1998) 5631–5635.
[2] S.W. Smith, G.C. Fu, J. Am. Chem. Soc. 131 (2009) 14231–14233.
[3] B.M. Trost, G.R. Dake, J. Am. Chem. Soc. 119 (1997) 7595–7596.
[4] C. Lu, X. Lu, Org. Lett. 4 (2002) 4677–4679.
[5] D. Virieux, A.-F. Guillouzic, H.-J. Cristau, Tetrahedron 62 (2006) 3710–3720.
[6] B.M. Trost, C.-J. Li, J. Am. Chem. Soc. 116 (1994) 10819–10820.
[7] Y.K. Chung, G.C. Fu, Angew. Chem., Int. Ed. 48 (2009) 2225–2227.
[8] M. Marigo, T.C. Wabnitz, D. Fielenbach, K.A. Jørgensen, Angew. Chem., Int. Ed. 44 (2005) 794–797.
[9] Y. Liu, B. Sun, B. Wang, M. Wakem, L. Deng, J. Am. Chem. Soc. 131 (2009) 418–419.
[10] M.H. Wu, E.N. Jacobsen, J. Org. Chem. 63 (1998) 5252–5254.
[11] J.R. Frauĭsto da Silva, R.J.P. Williams, The Biological Chemistry of the Elements, Oxford University Press, New York, 2001.
[12] Eds T. Toru, C. Bolm, Organosulfur Chemistry in Asymmetric Synthesis, Wiley-VCH, Weinheim, Germany, 2008.
[13] Ed H. Pellissier, Chiral Sulfur Ligands: Asymmetric Catalysis, Royal Society of Chemistry, Cambridge, U.K., 2009.
[14] J. Kang, J.B. Kim, J.W. Kim, D.J. Lee, Chem. Soc., Perkin Trans. 2 (1997) 189–194.
[15] J.C. Anderson, M. Harding, Chem. Commun. (1998) 393–394.
[16] C.E. Aroyan, S.J. Miller, J. Am. Chem. Soc. 129 (2007) 256–257.
[17] S. Fanjul, A.N. Hulme, J.W. White, Org. Lett. 8 (2006) 4219–4222.
[18] D. Enders, M.R.M. Hüttl, C. Grondal, G. Raabe, Nature 441 (2006) 861–863.
[19] W. Wang, H. Li, L. Wang, L. Zu, J. Am. Chem. Soc. 128 (2006) 10354–10355.
[20] B.M. Trost, C.-J. Li, J. Am. Chem. Soc. 116 (1994) 3167–3168.
[21] X. Lu, C. Zhang, Z. Xu, Acc. Chem. Res. 34 (2001) 535–544.
[22] J.L. Methot, W.R. Roush, Adv. Synth. Catal. 346 (2004) 1035–1050.
[23] J.W. Sun, G.C. Fu, J. Am. Chem. Soc. 132 (2010) 4568–4569.
[24] W. Tang, X. Zhang, Angew. Chem., Int. Ed. 41 (2002) 1612–1614.
[25] A. Milet, T. Korona, R. Moszynski, E. Kochanski, J. Chem. Phys. 111 (1999) 7727–7735.
[26] F.R. Clemente, K.N. Houk, Angew. Chem., Int. Ed. 43 (2004) 5766–5768.
[27] H. Sun, D.J. Zhang, F. Wang, C.B. Liu, J. Phys. Chem. A 111 (2007) 4535–4541.
[28] J. Wang, J.D. Gu, J. Leszczynski, M. Feliks, W.A. Sokalski, J. Phys. Chem. B 111 (2007) 2404–2408.
[29] T. Marcelli, P. Hammar, F. Himo, Chem. Eur. J. 14 (2008) 8562–8571.
[30] A.D. Becke, Phys. Rev. 38 (1988) 3098–3100.
[31] A.D. Becke, J. Chem. Phys. 98 (1993) 5648–5652.
[32] C. Lee, W. Yang, R.G. Parr, Phys. Rev. B 37 (1998) 785–789.
[33] M.J. Frisch, G.W. Trucks, H.B. Schlegel, G.E. Scuseria, M.A. Robb, J.R. Cheesman, J.A. Montgomery Jr., T. Vreven, K.N. Kudin, J.C. Burant, J.M. Millam, S.S. Iyengar, J. Tomasi, V. Barone, B. Mennucci, M. Cossi, G. Scalmani, G.A. Petersson, H. Nakatsuji, M. Hada, M. Ehara, K. Toyota, R. Fukuda, J. Hasegawa, M. Ishoda, T. Nakajima, Y. Honda, O. Kitao, H. Nakai, M. Klene, X. Li, J.E. Knox, H.P. Hratchian, J.B. Cross, C. Adamo, J. Jaramillo, R. Gomperts, R.E. Stratmann, O. Yazyev, A.J. Austin, R. Cammi, C. Pomelli, J. Otcherski, P.Y. Ayala, K. Morokuma, G.A. Voth, P. Salvador, J.J. Danneberg, V.G. Zakrzewski, S. Dapprich, A.D. Daniels, M.C. Strain, O. Farkas, D.K. Malick, A.D. Rabuck, K. Raghavachari, J.B. Foresman, J.V. Ortiz, Q. Cui, A. Baboul, S. Clifford, J. Cioslowski, B.B. Stefanov, G. Liu, A. Liashenko, P. Piskorz, I. Kamaromi, L.R. Martin, D.J. Fox, T. Keith, M.A. Al-Laham, C.Y. Peng, A. Nanaykkara, M. Challacombe, P.M.W. Gill, B. Johnson, W. Chen, M.W. Wong, G. Gonzalez, J.A. Pople, Gaussian 03, Revison B.03, Gaussian Inc., Pittsburgh, PA, 2003.
[34] A.D. Becke, J. Chem. Phys. 104 (1996) 1040–1046.
[35] Y. Zhao, B.J. Lynch, D.G. Truhlar, J. Phys. Chem. A 108 (2004) 2715–2719.
[36] K. Fukui, J. Phys. Chem. 74 (1970) 4161–4163.
[37] S.F. Boys, F. Bernardi, Mol. Phys. 19 (1970) 553–566.
[38] A.E. Reed, R.B. Weinstock, F. Weinhold, J. Chem. Phys. 83 (1985) 735–746.
[39] A.E. Reed, L.A. Curtiss, F. Weinhold, Chem. Rev. 88 (1988) 899–926.
[40] O. Tapia, J. Math. Chem. 10 (1992) 139–181.
[41] J. Tomasi, M. Persico, Chem. Rev. 94 (1994) 2027–2094.
[42] B.Y. Simkin, I. Sheikhet, Quantum Chemical and Statistical Theory of Solutions: A Computational Approach, Ellis Horwood, London, 1995.
[43] E. Cances, B. Mennunci, J. Tomasi, Chem. Phys. 107 (1997) 3032–3041.
[44] M. Cossi, V. Barone, R. Cammi, J. Tomasi, Chem. Phys. Lett. 255 (1996) 327–335.
[45] R. Hoffmann, Rev. Mod. Phys. 60 (1988) 601–628.
[46] D.G. Truhlar, B.C. Garrett, S.J. Klippenstein, J. Phys. Chem. 100 (1996) 12771–12800.
[47] D.Z. Chen, N. Lu, G.Q. Zhang, S.Z. Mi, Tetrahedron: Asymmetry 20 (2009) 1365–1368.
[48] K.B. Wiberg, Tetrahedron 24 (1968) 1083–1096.
[49] K. Sakota, Y. Shimazaki, H.J. Sekiya, Chem. Phys. 130 (2009) 1–4.